Available online at www.sciencedirect.com

SCIENCE DIRECT®

Combustion and Flame 145 (2006) 38–58

Combustion and Flame

www.elsevier.com/locate/combustflame

Formation of dark zone and its temperature plateau in solid-propellant flames: A review

Rongjie Yang, Piyush Thakre, Yeong-Cherng Liau, Vigor Yang *

Department of Mechanical and Nuclear Engineering, The Pennsylvania State University, 104 Research Building East, University Park, PA 16802, USA

Received 20 July 2005; received in revised form 28 November 2005; accepted 26 December 2005

Abstract

A comprehensive review on the formation of dark-zone temperature plateaus in solid-propellant flames has been conducted. Various key physiochemical processes involved in the formation of a dark zone were investigated for a broad range of propellants, including nitramine, ammonium dinitramide, and double-base propellants. The effects of propellant formulation, surface condition, burning rate, and preconditioned temperature, as well as ambient pressure and external stimuli, were investigated systematically. Dominant chemical pathways responsible for the formation of a dark zone were identified. Major species in the dark zone were tabulated for all the solid propellants of concern. Apart from NO, important species in a dark zone are CO for double-base, HCN for nitramine, and N_2O for ADN propellants. These chemical species typically undergo reactions with high activation energies and their chemical-induction and flow-residence times are instrumental in explaining the existence of a dark-zone temperature plateau. The transport velocity must be sufficiently high to allow for chemical species to travel farther from the propellant surface before they overcome the activation energies to react, thereby giving rise to a temperature plateau. Conversely, if the transport velocity is low, then reactions take place much closer to the propellant surface, producing a very short or even no dark zone. The flame stand-off distance decreases as the pressure increases because of the increase in the reactant concentrations and gas densities, which in turn increase the rate of reactions and reduce the transport velocity.

Keywords: Solid propellant combustion; Dark zone; Nitramine propellants; ADN propellant; Double-base propellants

1. Introduction

The "dark zone" in a solid-propellant flame is a nonluminous region which separates the primary reaction zone near the propellant surface from the luminous secondary flame zone. The existence of a dark zone is one of the distinctive visible characteristics observed in the combustion of many homogeneous solid propellants at low and moderate pressures. These include double-base (DB), nitramine (cyclotrimethylenetrinitramine, RDX, and cyclotetramethylenetetranitramine, HMX), and ammonium dinitride (ADN) propellants. Major species observed in the dark zone of DB propellant combustion are NO, CO, CO_2, N_2, H_2, and H_2O [1–3]. In addition, HCN is important in the dark zone of nitramine propellants [3–5] and N_2O in that of ADN propel-

---

* Corresponding author. Fax: +1 (814) 865 3389.
E-mail address: vigor@psu.edu (V. Yang).

doi:10.1016/j.combustflame.2005.12.005

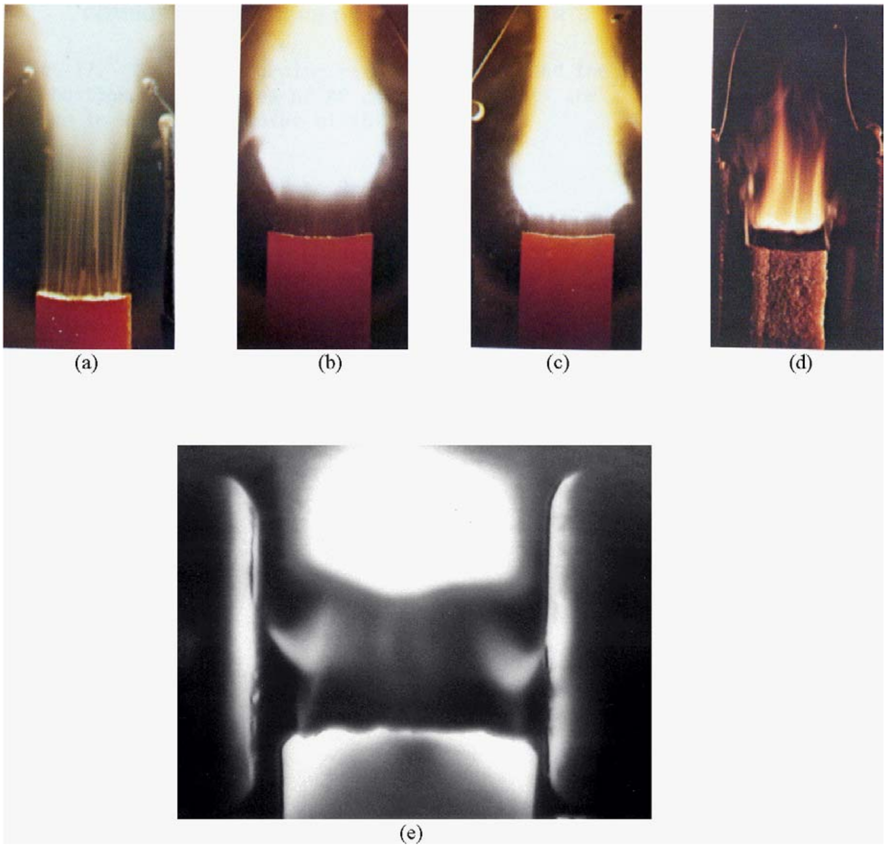

Fig. 1. Combustion of (a) DB propellant at 10 atm, (b) DB propellant at 20 atm, (c) DB propellant at 30 atm, (d) RDX composite propellant at 20 atm [2], and (e) XM39 propellant at 1 atm air [76].

lant [6–10]. In most cases, the dark zone exists in the range of 1–50 atm for DB and nitramine propellants and up to 40 atm for ADN. The latter has a lower temperature range of 850–1250 K, as compared to 1200–1600 K for DB and nitramine propellants. Fig. 1 shows photographs of flames exhibiting dark zones in the combustion of DB and RDX propellants. It is interesting to note that a dark zone may be present in the combustion of ammonium perchlorate (AP)/hydroxy-terminated polybutadiene (HTPB) propellant under subatmospheric pressures ($\sim 10^{-2}$ atm) [11].

To facilitate discussion, we first consider the combustion wave structure of RDX monopropellant under external laser heat flux, as shown schematically in Fig. 2. The condensed phase consists of a preheated zone and a multiphase layer underneath the propellant surface. The gas phase can conveniently be segmented into three regions: the primary flame, the dark zone, and the luminous secondary flame. During burning, the propellant remains thermally stable in the preheated zone until the temperature becomes high enough for melting and thermal decomposition in the subsurface multiphase layer. The decomposed species are ejected and transported away from the propellant surface via both diffusion and convection. Subsequent reactions occur among the decomposed products, and give rise to intermediate species such as HCN, NO, CO, and N_2O in the primary zone. The activation energies required for the reactions of these intermediate species are usually high, so that a finite reaction time is required and the species may travel a certain distance prior to the occurrence of exothermic reactions in the secondary flame. The temperature during the period of residence time usually ranges between 1200 and 1600 K, and the variations in the temperature and species concentrations are moderate. No significant visible emission is observed in this zone and thus it is referred to as the dark zone.

Even though it is commonly believed that a temperature plateau exists in the dark zone as shown in Fig. 2, the existence of such a plateau in the combustion of RDX monopropellant remains uncertain. Measurements of the temperature and species-concentration profiles by Parr and Hanson-Parr for RDX combustion [12,13], using nonintrusive planar

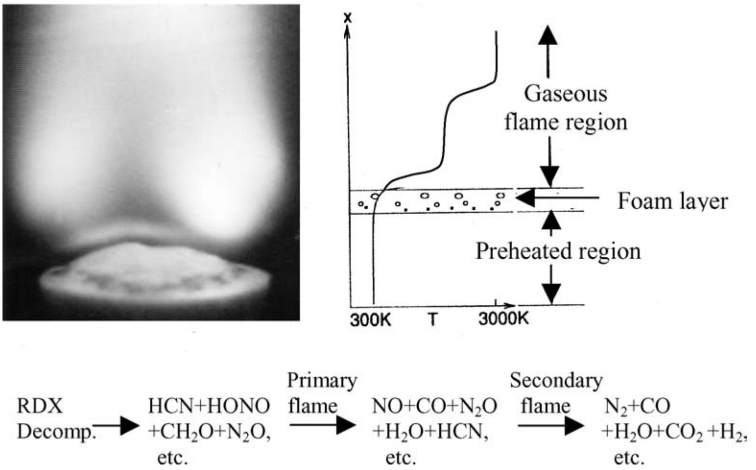

Fig. 2. Combustion-wave structure in laser-assisted combustion of RDX monopropellant.

laser-induced fluorescence (PLIF), UV/vis absorption, and thermocouple techniques, indicated that a temperature plateau exists in the case of laser-assisted deflagration (LAD) at 1 atm, but not in the case of self-sustained deflagration (SSD) at the same pressure. Lee et al. [14], in their temperature and species-concentration profile measurements using thermocouples and a triple-quadruple mass spectrometry (TQMS) technique, did not observe any temperature plateau between 1200 and 1600 K in either LAD or SSD of RDX. The temperature increased monotonically from the surface to its final value except for a short plateau around 600 to 700 K immediately above the propellant surface. They did, however, visually observe a dark zone in the LAD case [15]. Liau et al. conducted a comprehensive theoretical analysis of RDX monopropellant combustion [16,17]. The formulation accounts for detailed chemical kinetics and transport phenomena in the gas phase, and thermal decomposition and subsequent reactions in the condensed phase. The model predicted the existence of a temperature plateau for LAD [17], but not for SSD [16]. The temperature plateau was also predicted by other theoretical models for RDX combustion under external laser heating [18,19]. Results of these studies underline the fact that it may not always be precise to equate the dark zone to the temperature plateau. In this paper, the temperature plateau associated with the dark zone is referred to as the *dark-zone temperature plateau.*

The present work explains the mechanisms underlying dark-zone formation, and provides a comprehensive review of research efforts to date on the investigation of the dark zone and the associated temperature plateau. Dominant chemical pathways and physical processes responsible for the formation of a dark zone are identified for nitramine monopropellants, DB, and ADN propellants. Emphasis is placed on the effects of propellant formulation, surface condition, burning rate, and preconditioned temperature, as well as ambient pressure and external stimuli. Detailed descriptions of the key physiochemical mechanisms involved in dark-zone formation and its sensitivity to chemical and physical parameters for various solid propellants are discussed.

2. Mechanisms of dark-zone formation and ignition delay

The physiochemical processes in a dark zone can be globally characterized by two characteristic time scales accounting for the transport and chemical phenomena, respectively. The former, also referred to as the flow residence time τ_r, represents the time elapsed for a fluid element to travel through the dark zone, and is defined as

$$\tau_r = \frac{L_d}{V_d}, \tag{1}$$

where L_d is the dark-zone thickness and V_d is the local gas velocity. The mass continuity in the gas phase takes the form

$$V_d = \frac{r_b \rho_p}{\rho_g}, \tag{2}$$

where ρ_p is the propellant density, ρ_g the gas density, and r_b the burning rate of the propellant. Substitution of Eq. (2) into Eq. (1) for V_d and application of the equation of state result in the following equation for the flow residence time,

$$\tau_r = \frac{L_d p M}{R_u T_d \rho_p r_b}, \tag{3}$$

where T_d is the dark-zone temperature, M the mean gas molecular weight, R_u the universal gas constant, and p the pressure.

The chemical induction time τ_c, also known as the ignition delay time τ_d, is defined as the time interval between the generation of such major intermediate species as HCN, NO, CO, and N_2O at the end of the primary flame and their depletion at the beginning of the secondary flame. The reactions associated with these species usually have high activation energies, on the order of ∼45 kcal/mol. The species therefore need a finite period of residence time equal to the ignition delay time to complete the reactions at appropriate temperatures and pressures. The condition for the existence of a dark-zone temperature plateau and its overall properties can be determined by equating the two time scales: τ_r and τ_c. The chemical and transport characteristics of the intermediate species thus play a vital role in dictating the formation of a dark zone.

The dark-zone thickness is directly related to the ignition delay time and local gas velocity, as shown in Eq. (1). High burning rate and low gas density increase the gas velocity and cause the temperature plateau to be stretched, since the intermediate species can travel farther with the same ignition delay time τ_d. For most solid propellants, the pressure sensitivity of the burning rate can be expressed by the following Saint-Roberts law:

$$r_b = a_0 p^n. \tag{4}$$

Substitution into Eq. (2) leads to

$$V_d \sim \frac{r_b}{p} \sim p^{n-1}. \tag{5}$$

The chemical induction time or the ignition delay time depends on the ambient pressure in the following form:

$$\tau_c \sim p^{-r}. \tag{6}$$

Since $\tau_r = \tau_c$ to allow for the existence of a dark zone, the combination of Eqs. (5) and (6) with Eq. (1) results in the following relationship between the dark-zone thickness and pressure,

$$L_d = ap^d, \tag{7}$$

where the dark-zone pressure exponent d has a negative value, consistent with the observation that the length of a dark-zone decreases with increasing pressure. Equation (7) is identical to the expression originally proposed by Kubota and co-workers [20–25], based on the burning rate and flame-standoff distance (including the length of the primary flame zone) measured using high-speed microphotographs. The average global reaction rate in the dark zone is given by

$$\dot{\omega}_g = \frac{\rho_p r_b}{L_d} \sim p^k, \tag{8}$$

where the reaction order k is equal to $n - d$. Table 1 lists the pressure exponents, d and k, for a variety of DB and nitramine propellants. Experimental investigation of RDX and HMX combustion by Parr and

Table 1
Dark-zone pressure exponents and overall reaction orders for various solid propellants

Propellants	d	k	Ref.
NC/NG/HMX/DEP—catalyzed by lead stearate (PbSt)	−1.8 (noncatalyzed) −2.0 super-rate region −2.6 plateau region	2.6	[20]
RDX/PU = 80/20	−2.0	2.55	[22]
= 75/25	−2.3	2.81	
= 85/15	−2.0	2.6	
HMX/PU = 80/20	−1.9	2.54	
HMX (uncatalyzed)—catalyzed by PbSt + C	−2.0 −2.2	2.54 2.62	[23]
NC/NG/GAP = 50/40/10	−1.77	2.56	[25]
NC/NG/DEP = 50/40/10	−1.68	2.37	
GAP/HMX = 20/80—catalyzed by lead citrate + C	∼ −1.8 (uncatalyzed) ∼ −1.8 (fitting not good)		[21]
NC/NG/DEP = 25/65/10	−2.23	2.91	[24]
NC/NG/DEP + 16.7%HMX	−1.60	2.35	
NC/NG/DEP + 28.6%HMX	−1.64	2.40	
NC/NG/DEP + 44.4%HMX	−2.16	2.94	

Hanson-Parr [26] at pressures less than 0.5 MPa suggests an equation similar to Eq. (7),

$$L_d = a_1 p^{-1.02}. \qquad (9)$$

The modeling results of DB propellant combustion by Roh et al. [27] and Bizot and Beckstead [28] also supports the same functional relationship between $\log L_d$ and $\log p$. Fig. 3 shows the linear dependence of the flame-standoff distance on pressure in log–log coordinates (various propellants are summarized in Table 2). It is worth noting that the pressure exponents summarized in Table 1 are valid only in the pressure range of the measurements. In the limit of very low pressure, Eq. (7) does not hold since $L_d \to \infty$ as $p \to 0$. Self-sustained propellant combustion in general does not exist under this condition. Table 3 lists the first dark-zone properties of ADN propellant combustion with a preconditioned temperature of $T_i = 20\,°\mathrm{C}$ [6]. The pressure exponent of the dark-zone thickness d in Eq. (7) is around -0.6. The flame structure of ADN monopropellant will be detailed later.

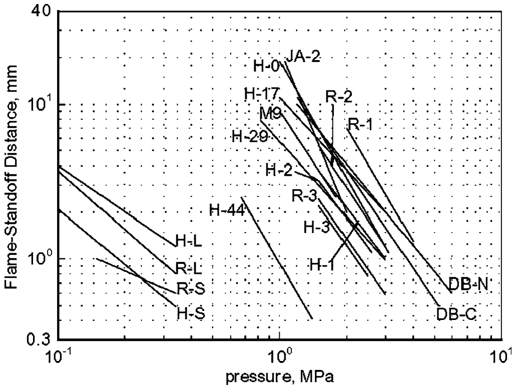

Fig. 3. Flame-standoff distance as function of pressure for various propellants (see Table 2).

Fifer et al. [29] and Ilincic et al. [30] conducted modeling studies using simplified skeletal and reduced chemical-kinetics mechanisms with prespeci-

Table 3

First dark-zone properties of ADN combustion at $T_i = 20\,°\mathrm{C}$ (Zenin et al. [6])

P, atm	5	10	20	30	40
L_d, mm	5	4	2.5	2.0	1.5
T_d, °C	700	800	950	1050	1200
$\dot{m}^a$, g/cm^2 s	2.40	2.88	3.36	4.00	4.64

[a] $\dot{m}$, burning rate.

Table 2

Code	Ingredient and composition	Remark	Ref.
DB-N	HMX—23%, NC—43%, NG—19%, DEP[a]—8%, SO[b]—7%	Noncatalyzed	[20]
DB-C	HMX—23%, NC—43%, NG—19%, DEP[a]—8%, SO[b]—7%	Catalyzed[c]	[20]
R-1	RDX—75%, PU[d]—20%	$d_L/d_S = 7/3$[e]	[22]
R-2	RDX—80%, PU[d]—25%	$d_L/d_S = 7/3$[e]	[22]
R-3	RDX—85%, PU[d]—15%	$d_L/d_S = 7/3$[e]	[22]
H-1	HMX—80%, PU[d]—20%	$d_L/d_S = 7/3$[e]	[22]
H-2	HMX[f]—80%, HTPE[g]—20%	Noncatalyzed	[23]
H-3	HMX[f]—80%, HTPE[g]—20%	Catalyzed[h]	[23]
H-0	HMX—0%, NC—25%, NG—65%, DEP[a]—10%	$d_{HMX} = 20$ µm	[24]
H-17	HMX—16.7%, NC—20.8%, NG—54.2%, DEP[a]—8.3%	$d_{HMX} = 20$ µm	[24]
H-29	HMX—28.6%, NC—17.9%, NG—46.4%, DEP[a]—7.1%	$d_{HMX} = 20$ µm	[24]
H-44	HMX—44.4%, NC—13.9%, NG—36.1%, DEP[a]—5.6%	$d_{HMX} = 20$ µm	[24]
R-L	RDX—100%	Laser-assisted[i]	[26]
R-S	RDX—100%	No laser	[26]
H-L	HMX—100%	Laser assisted[i]	[26]
H-S	HMX—100%	No laser	[26]
JA-2	NC—58%, NG—16%, DEGDN[j]—25%, others—1%	N_2 environment	[50]
M9	NC—58%, NG—40%, KNO_3—1.6%, others—0.4%	N_2 environment	[50]

[a] DEP: diethylphtalate.

[b] SO: sucrose octacetate.

[c] 3.2% lead stearate (PbSt: ~3 µm diameter).

[d] PU: polyurethane.

[e] d_L: large RDX particle size (120 µm), d_S: small RDX particle size (2 µm).

[f] Mixing ratio of large-size (220 µm) and small-size (20 µm) particles is 7/3.

[g] HTPE: hydroxy-terminated polyether.

[h] 2.4% PbSt + 0.4% C.

[i] CO_2-laser heat flux of 628 W/cm^2.

[j] DEGDN: diethylene glycoldinitrate.

fied dark-zone species concentrations to investigate the ignition delay times for DB and nitramine propellants under a broad range of pressure and temperature. For a typical DB propellant, Fifer et al. [29] obtained τ_d as a function of p and T_d in the range of 1–100 atm,

$$\tau_d = 4.5 \times 10^{-13} p^{-0.992} T_d^{2.992} \exp\left(\frac{31{,}140}{R_u T_d}\right) \text{ ms}, \tag{10}$$

where p is in atm and T_d in K. Zenin [31] measured the temperature fields and burning-rate properties using the micro-thermocouple technique for nitramine and DB propellants. A unified correlation for the ignition time delay was established for DB propellants of all the types in the pressure range of 20–50 atm,

$$\tau_d = 10^{7.2} p^{-2.4} \exp\left(\frac{-30{,}000}{R_u T_d}\right) \text{ ms}, \tag{11}$$

where p is in atm and T_d in K. The averaged dark-zone temperature T_d can be correlated with the final flame temperature T_f and pressure as follows [31],

$$T_d = 0.1566 T_f p^{0.350} + 645 \exp(-0.03p), \tag{12}$$

where T_f is in °C and p in atm.

3. Sensitivity of dark-zone formation to chemical pathways

3.1. Nitramine propellants

Much progress has been made in the past decade in the modeling and measurement of the combustion-wave structures and burning characteristics of nitramine monopropellants such as RDX and HMX, and pseudo-propellants such as RDX/GAP, HMX/GAP, and RDX/GAP/BTTN. All of the modeling work on RDX and HMX combustion employed the reaction mechanisms proposed by Melius [32] and Yetter et al. [33], to treat the gas-phase chemical kinetics. Melius' scheme (Melius90) consists of 38 species and 158 reactions, being derived by extending a generalized hydrocarbon/air flame model detailed by Miller and Bowman (MB89) [34]. The mechanisms include the oxidation of HCN, the conversion of NH_x species to NO and N_2, and the flame chemistry of C_2N_2/NO_2. Additional reactions are considered to model the decomposition of RDX and the subsequent reactions of the intermediate species. Yetter et al. (Yetter95) [33] adopted the same initial decomposition scheme for RDX monopropellants as that proposed by Melius, but used a modified set of subsequent reactions. The model was based on a hierarchical approach for collecting kinetic data and the specific chemical submodels that are required to form the gas-phase combustion mechanisms. In particular, three kinetic submodels of increasing complexity (N_2O decomposition, H_2/NO_2 reaction, and CH_4/N_2O reaction) are established in the Yetter95 model using the results from kinetic experiments over a broad range of temperature and pressure. The overall scheme considers 45 species and 232 reactions. Recently, Lin and co-workers established a chemical model (Lin99) [35] consisting of 49 species and 250 reactions for RDX combustion by adding reactions that involve the consumption of H_2CNNO_2, H_2CNNO, H_2CNO, and H_2CN. Table 4 lists the 20 new reactions added to the Yetter95 model. The rate constants of the four reactions marked by asterisks are revised, and two reactions involving the consumption of H_2CNNO_2 that enhance the ignition process are removed. The added reactions increase the initial consumption of H_2CN, but not H_2CNNO_2.

In the numerical analysis for RDX combustion developed by Liau and co-workers [16,17,36], the condensed-phase chemical process was modeled with two global decomposition reactions (R1) and (R2) and a subsequent reaction (R3). The exothermic reaction (R1) is favored under low heating-rate conditions, whereas the endothermic reaction (R2), also written as (R4) in [37], prevails at high temperatures. Among the intermediate products in the primary flame, the activation energies of reactions involving species like HCN and NO are usually high and their chemical and transport times must be commensurable to allow for the existence of a dark-zone temperature plateau. CH_2O and N_2O are highly reactive species, and reactions among them lead to the products H_2O, N_2, CO_2, and CO [36,37]. HONO and NO_2 tend to produce NO via the fast reactions (R5) and (R6) [37,38]. Thus (R2) and (R4) are likely to favor dark-zone formation, and (R7) involving N_2O is most likely to disfavor it.

$$\text{RDX}_l\ (\text{HMX}_l) \rightarrow 3(4)\ (CH_2O + N_2O), \tag{R1}$$

$$\text{RDX}_l\ (\text{HMX}_l) \rightarrow 3(4)\ (H_2CN + NO_2), \tag{R2}$$

$$CH_2O + NO_2 \rightarrow CO + NO + H_2O, \tag{R3}$$

$$\text{RDX}_l\ (\text{HMX}_l) \rightarrow 3(4)\ (\text{HCN} + \text{HONO}), \tag{R4}$$

$$H + NO_2 = NO + OH, \tag{R5}$$

$$H + \text{HONO} = NO + H_2O, \tag{R6}$$

$$H + N_2O = N_2 + OH. \tag{R7}$$

The sensitivity of dark-zone formation to the gas-phase chemical kinetics was also investigated by Liau and Yang [36] for RDX combustion. The chemical scheme was based on the Yetter95 mechanism, and the propellant surface condition was prespecified. The analysis was conducted by means of a modified damped Newton finite-difference method originally developed by Kee et al. [39]. The method combines both Newton-iteration and time-integration

Table 4
Comparison of gas-phase kinetics models of RDX combustion

Critical reactions in the Yetter95 model compared to the Melius90 model

Reactions	A[a]	E[a]
$H_2CNNO_2 + NO_2 = CH_2O + N_2O + NO_2$	1.00×10^{11}	2000.0
$H_2CNNO_2 + N_2O = CH_2O + N_2O + N_2O$	1.00×10^{11}	2000.0
$H_2COHNNO_2 \rightarrow HCN + NO_2 + H_2O$	1.00×10^{16}	0.0
$H_2CNNO\ (+M) = H_2CN + NO\ (+M)$	1.00×10^{16}	2000.0
$H_2CN + M = HCN + H + M$	5.30×10^{16}	29,000.0

Additional reactions in the Lin99 model

$H_2CNNO_2 \rightarrow H_2CN + NO_2$	$H_2CN + N_2O \rightarrow H_2CNO + N_2$[b]
$H_2CNNO_2 \rightarrow HONO + HCN$	$H_2CN + N_2O \rightarrow H_2CN_2 + NO$
$H_2CNNO_2 \rightarrow CH_2O + N_2O$	$H_2CN + NO_2 \rightarrow CH_2O + N_3$
$H_2CNNO \rightarrow HCN + HNO$	$H_2CN + NO \rightarrow HCN + HNO$[b]
$H_2CNNO \rightarrow CH_2O + N_2$	$H_2CN + NO \rightarrow H_2CNNO$
$H_2CNO \rightarrow HCN + OH$	$H_2CN + OH \rightarrow H_2CNOH$[c]
$H_2CNO \rightarrow HCNO + H$	$H_2CN + OH \rightarrow HCN + H_2O$
$H_2CN \rightarrow HCN + H$	$H_2CN + OH \rightarrow CH_3 + NO$
$H_2CN + NO_2 \rightarrow H_2CNNO_2$	$H_2CNOH \rightarrow HCN + H_2O$
$H_2CN + NO_2 \rightarrow HONO + HCN$[b]	$H_2CNOH \rightarrow H_2CN + OH$
$H_2CN + NO_2 \rightarrow CH_2O + N_2O$	$HCN + H_2O \rightarrow H_2CNOH$
$H_2CN + NO_2 \rightarrow H_2CNO + NO$[b]	

[a] $k = A\exp(-E/R_uT)$, k in s^{-1}, T in K, and E in cal/mol.
[b] Rate constants were revised.
[c] Declared duplicated reaction.

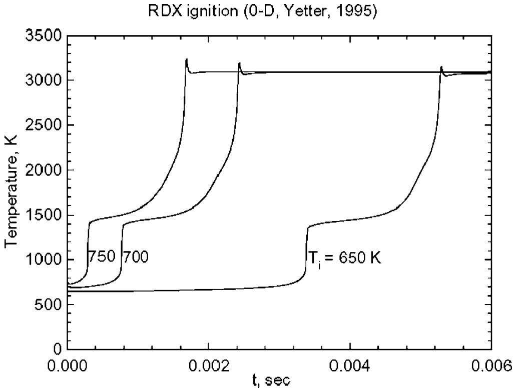

Fig. 4. Calculated temperature evolution of gaseous RDX ignition at various initial temperatures using the Yetter95 model.

techniques. Fig. 4 shows the calculated temperature evolution from a zero-dimensional homogeneous ignition study of RDX monopropellant for three different initial temperatures using the Yetter95 model, exhibiting a two-stage characteristic. Fig. 5 shows a comparison between the Yetter95 and Lin99 models for an initial temperature of $T_i = 700$ K. The latter predicts a longer ignition delay, indicating a slower heat-release rate in the gas phase near the surface.

Reactions (R7)–(R18) in the Yetter95 model consist of some of the major decomposition pathways,

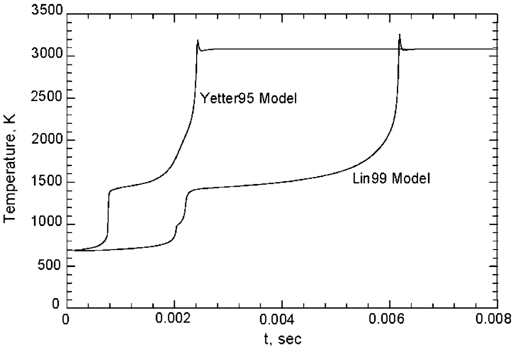

Fig. 5. Calculated temperature evolution of gaseous RDX ignition $T_i = 700$ K using the Yetter95 and Lin99 models.

conversions of major species in the dark zone, and reactions that exhibit strong effects on the temperature field and HCN production. The rate constant of each of (R7)–(R18) was artificially increased by a factor of 10, with all the other kinetic rates remaining unchanged, to examine the kinetic sensitivity. For (R8), the dark-zone thickness was shortened to about one-half. For (R9)–(R11), the dark zone completely disappeared with a 10-fold increase in the reaction rates, as shown in Fig. 6. Faster reactions of H_2CNNO_2 with NO_2, N_2O, and H_2O tend to eliminate the dark zone. This might be a reason that a dark-zone temperature plateau was observed in the laser-assisted

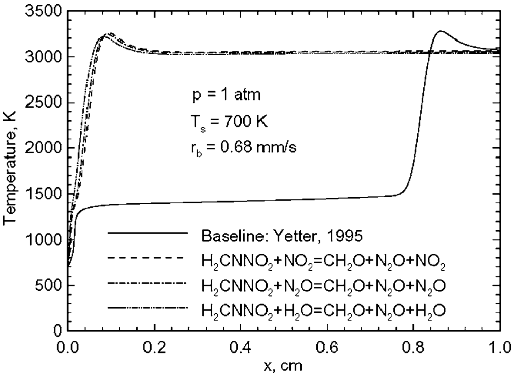

Fig. 6. Effect of initial decomposition pathway of RDX on temperature profile with a 10-fold increase of the rate constant.

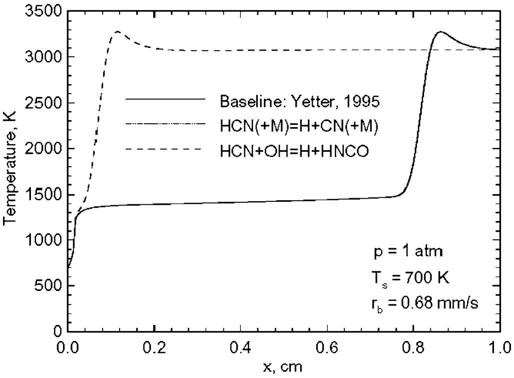

Fig. 7. Effect of a 10-fold increase of HCN reaction rate on temperature profile of RDX combustion.

deflagration of RDX monopropellant but not in the self-sustained deflagration, since the pathways (R9)–(R11) are favored without external heat flux. A trend similar to (R9)–(R11) was observed in Fig. 7 with (R13), whereas (R12) had a negligible effect on the temperature profile. Figs. 8 and 9 indicate that (R14)–(R17) did not affect the dark-zone thickness. Reactions (R12) and (R14) are unlikely to influence dark-zone formation as the energy required for the bond dissociation is quite high. The reaction channels producing HNCO seem to disfavor the dark-zone formation. Faster consumption of CH_2O does not affect the dark zone, possibly due to lower activation energies and large rate constants of (R16) and (R17). In contrast, (R18) and (R7) exert a significant influence on the dark-zone thickness and ignition delay, as evidenced in Fig. 10.

$$\mathrm{RDX}\ (+\mathrm{M}) = \mathrm{RDXR} + \mathrm{NO_2}\ (+\mathrm{M}), \tag{R8}$$

$$\mathrm{H_2CNNO_2} + \mathrm{NO_2} = \mathrm{CH_2O} + \mathrm{N_2O} + \mathrm{NO_2}, \tag{R9}$$

$$\mathrm{H_2CNNO_2} + \mathrm{N_2O} = \mathrm{CH_2O} + \mathrm{N_2O} + \mathrm{N_2O}, \tag{R10}$$

$$\mathrm{H_2CNNO_2} + \mathrm{H_2O} = \mathrm{CH_2O} + \mathrm{N_2O} + \mathrm{H_2O}, \tag{R11}$$

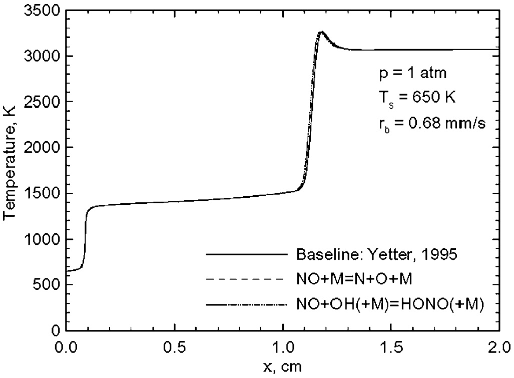

Fig. 8. Effect of a 10-fold increase of NO reaction rate on temperature profile of RDX combustion.

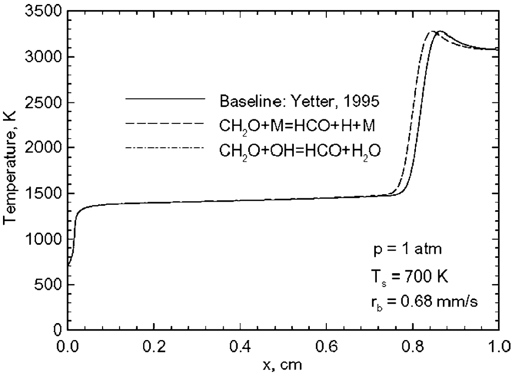

Fig. 9. Effect of a 10-fold increase of CH_2O reaction rate on temperature profile of RDX combustion.

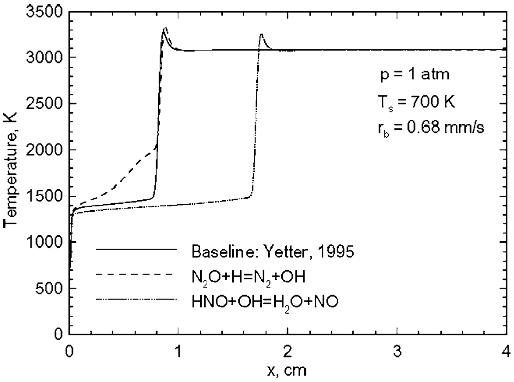

Fig. 10. Effect of a 10-fold increase of N_2O and HNO reaction rate on temperature profile of RDX combustion.

$$\mathrm{HCN}\ (+\mathrm{M}) = \mathrm{H} + \mathrm{CN}\ (+\mathrm{M}), \tag{R12}$$

$$\mathrm{HCN} + \mathrm{OH} = \mathrm{H} + \mathrm{HNCO}, \tag{R13}$$

$$\mathrm{NO} + \mathrm{M} = \mathrm{N} + \mathrm{O} + \mathrm{M}, \tag{R14}$$

$$\mathrm{NO} + \mathrm{OH}\ (+\mathrm{M}) = \mathrm{HONO}\ (+\mathrm{M}), \tag{R15}$$

$$\mathrm{CH_2O} + \mathrm{M} = \mathrm{HCO} + \mathrm{M}, \tag{R16}$$

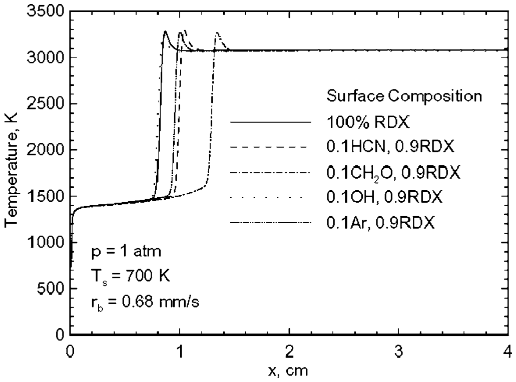

Fig. 11. Effect of surface composition on temperature profile of RDX combustion.

$$CH_2O + OH = HCO + H_2O, \quad (R17)$$

$$HNO + OH = H_2O + NO. \quad (R18)$$

Fig. 11 shows the effect of the surface composition on the temperature profile based on the Yetter95 model [36]. An artificial addition of inert gas such as argon extends the dark zone, due to the dilution of reactant species. Addition of HCN also increases the flame-standoff distance. This phenomenon may result from the high activation energy for the conversion of HCN, and the reduction in the concentrations of other species. Conversely, the addition of OH radical slightly decreases the flame-standoff distance, since this radical is reactive and requires less activation energy to initiate reactions with other species. The presence of 10% CH_2O increases the dark-zone thickness by 60%. The rapid volume dilatation arising from the highly exothermic reaction of CH_2O and NO_2 (R3) tends to increase the local flow velocity, and consequently extends the dark zone.

The theoretical calculations by Ermolin et al. [40] for RDX combustion revealed the importance of (R19) and (R20). When these two reactions were removed, a dark zone was observed which indicates that (R19) and (R20) are likely to disfavor the formation of a dark zone. NH_2 is produced mainly through (R21). This observation is consistent with the aforementioned sensitivity analysis that a 10-fold increase in the rate of (R13) completely eliminates the dark zone. The HNCO species in (R13) thus plays a crucial role in determining the formation of a dark zone.

$$NH_2 + NO = N_2H + OH, \quad (R19)$$

$$N_2H + NO = HNO + N_2, \quad (R20)$$

$$HNCO + H = NH_2 + CO. \quad (R21)$$

Ilincic et al. [30] investigated the structure of the dark zone in nitramine propellant combustion with four different chemical-kinetics mechanisms. The initial species composition was prespecified as NO (13%), HCN (22%), CO (22%), CO_2 (8%), N_2 (8%), H_2 (7%), H_2O (20%), and N_2O (0 or 2%). The four mechanisms included a detailed mechanism with 41 species and 190 reactions, a skeletal mechanism with 17 species and 23 reactions, and two reduced mechanisms with 10 species and 6 reactions (six-step mechanism), and 8 species and 4 reactions (four-step mechanism). The latter two mechanisms consist of (R22)–(R27) and (R25) + (R28)–(R30), respectively. The ignition-delay times calculated using the skeletal mechanism are found to agree reasonably well with those calculated using the detailed kinetics. The ignition-delay times and structures of the dark zones calculated using the reduced six-step mechanism are in agreement with those using the skeletal mechanism, but the four-step reduced mechanism predicts significantly shorter ignition-delay times:

six-step,

$$2NO + 2H_2 = N_2O + 2H + H_2O, \quad (R22)$$

$$H_2O + HCN = H_2 + HNCO, \quad (R23)$$

$$N_2O + 2H_2 = N_2 + 2H + H_2O, \quad (R24)$$

$$CO + H_2O = CO_2 + H_2, \quad (R25)$$

$$2H + M = H_2 + M, \quad (R26)$$

$$NO + H + HNCO = N_2O + CO + H_2; \quad (R27)$$

four-step,

$$2NO + H_2 = N_2O + H_2O, \quad (R28)$$

$$N_2O + H_2 = N_2 + H_2O, \quad (R29)$$

$$CO + H_2O = CO_2 + H_2, \quad (R25)$$

$$NO + H_2O + HCN = N_2O + CO + 1.5H_2. \quad (R30)$$

Vanderhoff et al. [41] performed a numerical investigation for the ignition delay of nitramine propellants using a modified MB89 model. On removing (R31) and (R32) from the mechanism, the ignition delay for HMX2 (80% HMX, 20% PU binder) increased from 34.6 ms to 1.85 s. Anderson et al. [38] noted that the calculated rate coefficient of the reverse reaction of (R31) ($A = 1.9 \times 10^{11}\ s^{-1}$, $E = 3400$ cal/mol) used in the MB89 mechanism was not accurate, and suggested that (R31) not be included in the dark-zone modeling as its rate under combustion condition is negligible.

$$N + CO_2 = NO + CO, \quad (R31)$$

$$HNO + NO = N_2O + OH. \quad (R32)$$

In the current paper, the effects of the reactions listed in Table 5 on the ignition delay of gaseous RDX in a well-stirred reactor were explored using the Lin99

Table 5
Ignition delay time (ms) of RDX in a well-stirred reactor based on the Lin99 model

Reactions	Modification	τ_d, ms	$\tau_d - \tau_0$, ms[a]
$N + CO_2 = NO + CO$ (R31)	Removed	6.2676	0.1332
	10 × k	5.3054	−0.8290
$HNO + NO = N_2O + OH$ (R32)	Removed	6.3529	0.2185
	10 × k	5.0011	−1.1333
$NH_2 + NO = N_2H + OH$ (R19)	Removed	7.5980	1.4636
	10 × k	4.2574	−1.8770
$NH_2 + NO = N_2 + H_2O$ (R33)	Removed	4.2824	−1.8520
	10 × k	7.5467	1.4123
$N_2H + NO = N_2 + HNO$ (R20)	Removed	6.0958	−0.0386
	10 × k	6.1966	0.0622
$N_2O + O = NO + NO$ (R48)	Removed	6.1359	0.0015
	10 × k	6.1227	−0.0117
$HCN = HNC$ (R36)	Removed	7.1226	0.9882
	10 × k	6.1059	−0.0285
$HCN + OH = HNCO + H$ (R13)	Removed	6.1628	0.0284
	10 × k	5.9279	−0.2047
$HNC + OH = HNCO + H$ (R34)	Removed	7.9870	1.8526
	10 × k	5.0612	−1.0732
$HCN + NO_2 = HNCO + NO$	Removed	6.1344	0
	10 × k	6.1342	−0.0002
$NCO + CH_2O = HNCO + HCO$	Removed	6.1342	−0.0002
	10 × k	6.1442	0.0098
$NCO + HNO = HNCO + NO$	Removed	6.1225	−0.0119
	10 × k	6.2258	0.0914
$NCO + HONO = HNCO + NO_2$	Removed	6.1338	−0.0006
	10 × k	6.1305	−0.0039
$HOCN + H = HNCO + H$	Removed	6.2475	0.1131
	10 × k	6.0776	−0.0568
$HNCO + H = NH_2 + CO$ (R21)	Removed	7.6643	1.5299
	10 × k	4.8828	−1.2516
$HNCO + OH = H_2O + NCO$	Removed	6.0460	−0.0884
	10 × k	6.4438	0.3094
$HNCO + CN = HCN + NCO$ (R35)	Removed	5.8689	−0.2655
	10 × k	6.4228	0.2884
$HNCO + NH_2 = NH_3 + NCO$	Removed	6.1245	−0.0099
	10 × k	6.1997	0.0653
$HNCO + O = CO_2 + NH$	Removed	6.1338	−0.0004
	10 × k	6.1395	0.0051
$HNCO + O_2 = HNO + CO_2$	Removed	6.1344	0
	10 × k	6.1343	−0.0001
$HNCO + NH = NH_2 + NCO$	Removed	6.1343	−0.0001
$HNCO + HO_2 = NCO + H_2O_2$	Removed	6.1334	−0.0010

[a] Ignition delay time based on the Lin99 model, $\tau_0 = 6.1344$ ms at 1 atm.

model [35] at 1 atm. Table 5 shows the calculated ignition delay time for the case when either each of these reactions was removed or its rate constant was artificially increased by a factor of 10. The removal of either (R31) or (R32) has a negligible influence on the ignition delay with a small deviation of 0.1–0.2 ms from the baseline case. A 10-fold increase in the rate constant, however, results in a noticeable decrease (around 1 ms) in the ignition delay. The importance of the (R31) and (R32) indeed depends on their rate constants. Reactions (R19) and (R33) are vital in affecting the ignition delay. Reaction (R19) tends to facilitate the ignition delay whereas (R33) exerts an opposite trend. Reaction (R20) has no significant effect on the ignition delay. Among all the reactions involving HNCO in the Lin99 model, (R21) and (R34) are the most sensitive ones, and significantly shorten the ignition delay. In addition, (R13) tends to slightly decrease the ignition delay, while (R35) exerts an opposite trend. Rearrangement of HCN to HNC (R36) was also found to be important. In summary, the reactions most critically affecting the dark-zone formation in nitramine propellant combustion include (R9)–(R11), (R19)–(R21), and (R31)–(R36).

$$NH_2 + NO = N_2 + H_2O, \tag{R33}$$

$$HNC + OH = HNCO + H, \tag{R34}$$

$$HNCO + H = NH_2 + CO, \tag{R21}$$

$$HCN + OH = HNCO + H, \tag{R13}$$

$$HNCO + CN = HCN + NCO, \tag{R35}$$

$$HCN = HNC. \tag{R36}$$

Tables 6–9 summarize the measured and predicted chemical compositions in the dark zones of RDX, HMX, and nitramine-based composite propellants [3,13,18,41–53]. Good agreement is achieved between experimental measurements [14] and model predictions [17,18]. The major species in the dark zone are NO and HCN, and the CO concentration is about 10%, except for the cases involving BAMO. The NO concentrations under laser-assisted conditions are higher than their counterparts under self-assisted deflagration. Homan et al. [54] performed an experimental study using absorption spectroscopy, along with a numerical analysis based on the Yetter95 model, on self-deflagrating RDX in air at 1 atm. The measured and predicted peak mole fractions of

Table 6
Measured and predicted molar concentrations in the dark zone of RDX and HMX combustion at 1 atm

Propellant	NO	HCN	CO	CO_2	H_2O	N_2O	NO_2	N_2	CH_2O	H_2	Ref.
RDX[a] $L_d = 0.5$ mm, $\dot{q}''_{laser} = 100$ W/cm^2	0.21	0.22	0.1	0.02	0.26	0.05	0.0	0.05	0.02	0.05	[14]
RDX[a] $L_d = 1$ mm, $\dot{q}''_{laser} = 400$ W/cm^2	0.23	0.22	0.1	0.01	0.26	0.04	0.0	0.04	0.02	0.05	[14]
RDX[a,c] $L_d \sim 1$ mm, $\dot{q}''_{laser} = 600$ W/cm^2	0.2						0.045				[13]
RDX[b,d] $L_d = 2$ mm, $\dot{q}''_{laser} = 400$ W/cm^2	0.30	0.215	0.10		0.20	0.045		0.04		0.03	[17]
RDX[b,e,f] $L_d = 1$ mm,	0.29	0.25	0.09	0.028	0.24	0.062	0	0.033	0.005	0.028	[18]
HMX[b] $L_d = 2.25$ mm, $\dot{q}''_{laser} = 100$ W/cm^2	0.2	0.2	0.07	0.03	0.2	0.05	0.05	0.1	0.07	0.03	[42]
HMX[b] $L_d = 3.5$ mm, $\dot{q}''_{laser} = 300$ W/cm^2	0.25	0.21	0.08	0.02	0.21	0.1	0.01	0.08	0.02	0.03	[42]
HMX[b,f] $L_d = 1$ mm	0.26	0.225				0.09	~0				[48]

[a] Experimental measurement.
[b] Numerical modeling.
[c] $T_d \sim 1600$ K.
[d] $T_d = 1500$ K.
[e] $T_d = 1360$ K.
[f] Self-sustained deflagration.

Table 7
Measured mole fractions of dark-zone species for self-sustained combustion of XM39[a], HMX-2[b], and M43[c] propellants

Propellant	NO	HCN	CO	CO_2	H_2O	N_2O	NO_2	CH_4	Ref.
XM39 (10–12 atm) $L_d = 1.5$ mm $T_d = 1150$ K	0.15	0.14	0.12	0.04	0.15	$\leqslant 0.02$		~ 0.005	[3]
XM39 (1 atm) $L_d = 2$ mm $T_d = 1300$ K	0.082								[49]
XM39 (6 atm) $L_d \sim 1$ mm	0.25 ± 0.05					0.15 ± 0.10	0.10 ± 0.05		[51]
HMX-2 (19 atm) $T_d = 1310$ K	0.13								[41]
M43 (11 atm) $L_d = 3$ mm $T_d = 1200$ K	0.22								[50]

[a] XM39: RDX (76%), cellulose acetate butyrate (CAB) (12%), acetyl triethyl citrate (ATEC) (7.6%), NC (4%).
[b] HMX-2: HMX (80%), PU binder (20%).
[c] M43: RDX (76%), CAB (12%), NC (4%), and energetic plasticizer (8%).

Table 8
Measured mole fractions of dark-zone species for laser-assisted combustion of XM39, M43, and RDX–CAB propellants

Propellant	NO	HCN	CO	CO_2	H_2O	N_2O	NO_2	N_2	CH_2O	H_2	Ref.
XM39 (3 atm)[a,b] $L_d = 3$ mm $\dot{q}''_{laser} = 100\ \mathrm{W/cm^2}$	0.19	0.16			0.20		0.005		0.045		[52]
XM39 (1 atm)[a] $L_d = 3$ mm $\dot{q}''_{laser} = 400\ \mathrm{W/cm^2}$	0.21	0.185			0.2	0.08	0.055		0.005	0.02	[52]
XM39 (1 atm)[a] $L_d = 3$ mm $\dot{q}''_{laser} = 400\ \mathrm{W/cm^2}$	0.28	0.12	0.07		0.19	0.08	0.1		0.17		[45]
XM39 (3 atm)[a] $L_d = 3$ mm $\dot{q}''_{laser} = 400\ \mathrm{W/cm^2}$	0.31	0.19	0.08	0.05	0.17	0.06	0.001	0.075	0.06	0.001	[45]
XM39 (1 atm) $L_d = 4$ mm $\dot{q}''_{laser} = 350\ \mathrm{W/cm^2}$	0.12						~ 0				[49]
M43 (1 atm)[a,c] $\dot{q}''_{laser} = 400\ \mathrm{W/cm^2}$	0.265	0.195			0.135	0.085	0.005		0.005	0.02	[52]
RDX–CAB (3 atm)[a,d] $L_d = 1.5$ mm $\dot{q}''_{laser} = 400\ \mathrm{W/cm^2}$	0.25	0.15	0.1	0.03	~ 0.27	0.01	~ 0	0.08	0.02	0.04	[45]

[a] In argon.
[b] $T_d = 1200$ K.
[c] $T_d = 1230$ K.
[d] $T_d = 1300$ K.

NO were 0.25 at 0.1 mm and 0.26 at 0.09 mm from the propellant surface, respectively. The modeling result also showed good agreement with that from the Liau and Yang [16] model, with an NO peak mole fraction of 0.21 at 0.13 mm from the propellant surface.

Table 9
Measured and predicted mole fractions of dark-zone species for laser-assisted combustion of RDX, HMX/GAP, and BAMO propellants at 1 atm

Propellant	NO	HCN	CO	CO_2	H_2O	N_2O	NO_2	N_2	CH_2O	H_2	CH_4	Ref.
GAP/HMX[a,c] $L_d = 2$ mm $\dot{q}''_{laser} = 100\ W/cm^2$ $T_d = 1400$ K	0.17	0.28	0.10	0.03	0.16	0.08	∼0	0.12	0.045		0.002	[46]
GAP/HMX[b,c] $L_d = 2$ mm $\dot{q}''_{laser} = 400\ W/cm^2$ $T_d = 1500$ K												[47]
GAP/RDX[a,c] $L_d = 2$ mm $\dot{q}''_{laser} = 100\ W/cm^2$ $T_d = 1360$ K	0.07	0.19	0.175	0.035	0.22	0.02	∼0	0.23	0.02		0.05	[46]
GAP/RDX[b] $L_d = 1$ mm $\dot{q}''_{laser} = 100\ W/cm^2$ $T_d = 1350$ K	0.24	0.255	0.065	0.035	0.22	0.05	0	0.08	0	0.005		[53]
BAMO/RDX[a,c] $L_d = 2$ mm $\dot{q}''_{laser} = 100\ W/cm^2$ $T_d = 1200$ K	0.2	0.2	0.02	0.02	0.05	0.08	0.005	0.095	0.015		0.006[d]	[43]
BAMO/RDX[a,c] $L_d = 2$ mm $\dot{q}''_{laser} = 400\ W/cm^2$ $T_d = 1500$ K	0.2	0.195	0.02	0.07	0.045	0.04	0.02	0.14	0.01	∼0.02	0.006[d]	[43]

[a] Experimental measurement.
[b] Numerical modeling.
[c] In argon.
[d] $C_2H_4 + C_2H_2 + CH_4$.

At the end of the dark zone, NO and HCN are consumed rapidly to produce N_2 and CO. The concentrations of radicals CN, NH, and OH increase sharply and a luminous flame appears. NH and CN radicals show a maximum concentration peak near the burning surface, while the concentration of OH remains nearly constant, except for a sharp increase in the primary flame zone. For RDX and HMX, the predicted profiles of CN, NH, and OH concentrations agree reasonably well with the measurements [13,19,20,54,55].

Table 9 summarizes the dark-zone properties of nitramine pseudo-propellants with energetic binders. For HMX/GAP and RDX/GAP binary pseudo-propellants, the concentration of HCN seemed to be higher than NO [46]. As with other nitramine-based composite propellants, the addition of GAP into HMX and RDX lengthens the dark zone and decreases the extent of the primary reaction zone [51]. Litzinger and co-workers observed the existence of a dark-zone temperature plateau in RDX/BAMO combustion [43]. RDX/BAMO burned unluminously at 1 atm with a laser flux of 100 W/cm^2, whereas an unstable luminous flame appeared at 400 W/cm^2.

3.2. Double-base propellants

It is well established that the thermal decomposition of nitrocellulose (NC) and nitroglycerin (NG) in the condensed phase of a DB propellant produces RCHO and NO_2 [1]. Reactions between aldehydes and NO_2 further produce NO, CH_2O, CO, and CO_2 [27,28]. In the primary flame zone immediately above the propellant surface, (R37) is dominant, and (R38)–(R40) of $CH_2O + CH_2O$, $(CHO)_2 + (CHO)_2$, and NO + C also occur. In the secondary flame zone, (R41) is the major reaction contributing to the formation of final products. It should be noted that (R37)–(R41) are not the elementary reaction steps.

$$NO_2 + CH_2O \rightarrow NO + CO + CO_2 + H_2O, \qquad (R37)$$

$$CH_2O + CH_2O \rightarrow CO + C_2H_4 + H_2O, \qquad (R38)$$

$$(CHO)_2 + (CHO)_2 \rightarrow 4CO + 2H_2, \qquad (R39)$$

$$NO + C \rightarrow N_2 + CO, \tag{R40}$$

$$NO + CO \rightarrow N_2 + CO_2. \tag{R41}$$

Ilincic et al. [30] performed a numerical study on the dark-zone structures of DB propellants using a well-stirred model for various initial pressures and temperatures. The initial dark-zone composition was set to be NO (24%), CO (33%), CO_2 (10%), N_2 (4%), H_2 (8%), and H_2O (20%). Three chemical-kinetics schemes were employed: a detailed mechanism consisting of 41 species and 190 reactions, a skeletal mechanism including 15 species and 22 reactions, and a three-step reduced mechanism represented by reactions (R25), (R28), and (R29). The predicted τ_d based on the three mechanisms were 0.1142, 0.1147, and 0.1142 s, respectively, for $T_d = 1400$ K and $p = 5$ atm. It was found that the temperature and species-concentration profiles using the reduced mechanism agree closely with those calculated using the skeletal mechanism, except for times close to ignition. The simplified mechanisms performed better for DB propellants than for nitramine propellants, a fact attributed to the higher chemical complexity of the latter.

Fifer et al. [29] used a four-step global mechanism (R42)–(R45) to predict the ignition delay for DB propellants. The rate coefficients of the four global reactions were obtained empirically and the predicted ignition-delay times agreed well with those predicted using a detailed kinetic mechanism involving 234 reactions. The model, however, used the kinetic parameters for (R31) which were not accurate [38].

$$NO + M = N + O + M, \tag{R42}$$

$$N + N + M = N_2 + M, \tag{R43}$$

$$O + CO + M = CO_2 + M, \tag{R44}$$

$$H_2 + CO_2 = H_2O + CO. \tag{R45}$$

Miller and Anderson [56,57] studied various dark-zone properties in the combustion of NG. The initial overall decomposition pathway of NG in the condensed phase was (R46). At 10 atm, L_d and T_d for NG propellant combustion were 10 mm and 1700 K, respectively. On adding 5.3 and 10% NH_3 to NG, L_d decreased to 8 and 3.5 mm, respectively, whereas the burning rate and T_d increased. On the other hand, when HNCO was added to NG, both L_d and the burning rate decreased. The addition of HNCO caused the global reaction rate to decrease in the primary flame, but increase in the dark zone. The phenomenon may be attributed to the fact that the OH/H concentration ratio favors the production of OH near the surface and H in the dark zone. Consequently, different HNCO pathways dominated and affected the radical pool, as explained in detail in Ref. [56]. Adding 2.7% CH_2O to NG decreased the burning rate and increased L_d slightly. The addition of NH_3 increased the heat feedback from the gas phase to the surface, whereas HNCO and CH_2O decreased such heat feedback. The decrease in L_d can be attributed to the reduction of NO by NH_3 and HNCO. The heat release rate in the dark zone was enhanced with (R19), (R21), (R33), and (R47). The combustion of M30 propellant (NC 29%, NG 22%, nitroguanidine (NQ) 47%, stabilizer 2%) exhibited no dark zone, possibly due to the substantial amount of NH_3 produced by NQ decomposition.

$$NG \rightarrow 2NO_2 + HONO + 2CH_2O + CO, \tag{R46}$$

$$NH_3 + OH = NH_2 + H_2O. \tag{R47}$$

Vanderhoff et al. [41] studied numerically the influences of (R31) and (R32) on τ_d for DB propellants using a modified MB89 model. The measured and predicted ignition delay times were 3.6 and 1.7 ms, respectively. When either (R31) or (R32) was removed, τ_d became 5.4 or 2.6 ms, respectively. If both reactions were excluded, τ_d increased to 23 ms, indicating that (R31) and (R32) are the key reactions in the dark zone. Anderson et al. [38], however, pointed out that (R31) was not important in the dark zone. In addition, the dark-zone formation for DB propellants was moderately sensitive to (R48) [58]. In short, the key reactions in the dark zone were (R32) and (R48). Small amounts of NO_2, CH_2O, NH_3, CH_4, and C_2H_4 in the dark zone may shorten its length.

$$N_2O + O = NO + NO. \tag{R48}$$

Table 10 summarizes the measured and predicted species compositions and temperatures in the dark zones of DB propellants [3,8,27,41,59,60]. The NO mole fraction was in a range similar to that for nitramine propellants, but the CO concentration was higher for DB propellants. HCN was absent in the dark zone of DB propellants. Under the laser-assisted combustion of JA-2 (NC 58.2%, NG 15.8%, DEGDN 35.2%) and M-9 (NC 57.6%, NG 40%), the NO mole fraction in the dark zone seemed very high (about 33%) [41,59].

The dark-zone chemistry of DB propellants appears to be less complicated than that of nitramine propellants, due to the absence of species HCN. In general, the chemical-kinetics models for DB propellants lead to results in good agreement with experimental measurements. The reduced four-step [29] and three-step [30] mechanisms predicted the ignition delay characteristics reasonably well, with an average deviation of 5% from the results using the detailed mechanisms. The simplified mechanisms, however, failed to predict the ignition delay time closely for nitramine propellants, with an average error of about

Table 10
Measured and predicted mole fractions of dark-zone species for self-sustained and laser-assisted combustion of DB, JA-2[a], M-9[b], M-10[c] propellants

Propellant	NO	HCN	CO	CO_2	H_2O	N_2	NO_2	H_2	CH_2O	CH_4	C_2H_4	Ref.
DB-1 (16 atm)[d] $T_d = 1600$ K	0.24	0.004	0.33	0.10	0.20	0.04		0.08		0.008	0.008	[3,44]
JA-2 (10 atm)[d] $T_d = 1400$ K	0.22	0	0.38	0.11	0.23					~0.005	0	[3,50]
JA-2 (1 atm)[d,e] $T_d = 1820$ K	0.33		0.33	0.095	0.14	0	0.015	0.025	0.065			[41]
M-9 (16 atm)[d] $T_d = 1500$ K	0.30											[59]
M-9 (1 atm)[d,e] $T_d = 1900$ K	0.33		0.33	0.11	0.16	0	0.003	0.043	0.024			[59]
M-10 (11.3–18.9 atm)[d] $T_d = 1325 \pm 75$ K	0.145 ± 0.015											[59]
DB (15 atm)[d] $L_d = 6$ mm $T_d = 1480$ K	0.065		0.38	0.15	0.09	0.1		0.25				[8]
DB (11 atm)[d] $T_d = 1700$ K	0.26		0.34	0.18	0.14	0.04		0.007				[60]
DB (10 atm)[f] $T_d = 1600$ K	0.25		0.33	0.21	0.135	0.03		0.006				[27]

[a] JA-2 (NC 58.2%, NG 15.8%, DEGDN 35.2%).
[b] M-9 (NC 57.6%, NG 40%).
[c] M-10 (98% NC).
[d] Experimental measurement.
[e] Laser-assisted combustion with $\dot{q}''_{\text{laser}} = 100\ \text{W/cm}^2$.
[f] Numerical modeling.

15% as compared with the detailed mechanisms. The rate constants of elementary and global reactions exert a significant effect on the modeling results.

3.3. ADN propellant

The combustion of ADN propellant exhibits several distinct characteristics, including a substantial heat release in the condensed phase and a weak heat feedback from the gas phase. The ADN decomposition process is assumed to be initiated by (R49)–(R51), followed by (R52)–(R56) among the subsequent decomposition products [9,10,61–64]. In the primary flame, along with (R52)–(R56), $NH_3 + NO_x$ and $NH_2 + NO_x$ are the main reactions [9,10,61–64].

$$\text{ADN} \rightarrow NH_3 + HN(NO_2)_2, \quad \text{(R49)}$$

$$\text{ADN} \rightarrow NH_3 + HNO_3 + N_2O, \quad \text{(R50)}$$

$$\text{ADN} \rightarrow NH_4NO_3 + N_2O, \quad \text{(R51)}$$

$$HN(NO_2)_2 \rightarrow HNO_3 + N_2O, \quad \text{(R52)}$$

$$HN(NO_2)_2 \rightarrow HNNO_2 + NO_2, \quad \text{(R53)}$$

$$NH_3 + HNO_3 \rightarrow NH_4NO_3, \quad \text{(R54)}$$

$$HNNO_2 + NO_2 = HNO + NO + NO_2, \quad \text{(R55)}$$

$$HNNO_2 \rightarrow N_2O + OH. \quad \text{(R56)}$$

The combustion wave of ADN exhibits a two-zone flame structure in the pressure range of 5–20 atm [6]. Below 3 atm, the secondary flame was not seen. Fig. 12 shows the predicted temperature and species-concentration profiles above the propellant surface at 6 atm, where the primary flame is not shown [65]. The analysis contains a gas-phase chemical kinetics scheme of 33 species and 180 reactions, using the measured surface compositions as an input. The first dark-zone temperature plateau is seen around 900 K, followed by a secondary flame with a sharp increase from 1000 to 1500 K. The second dark-zone temperature plateau occurs around 1500 K at the end of the secondary flame. Reactions continue beyond the second dark zone until the final adiabatic temperature is reached. According to the experimental results of Zenin et al. [6] and Fogelzang et al. [10], at 5–20 atm, the first dark-zone temperature plateau is in the range

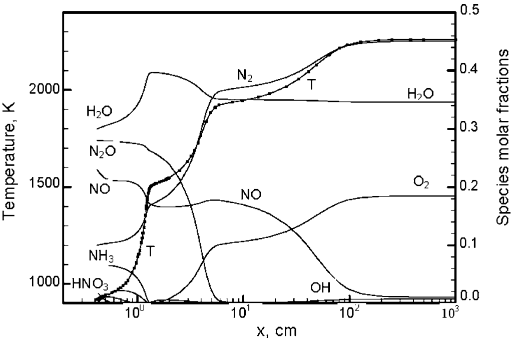

Fig. 12. Predicted profiles of temperature and species concentrations in the ADN flame above propellant surface at 6 atm.

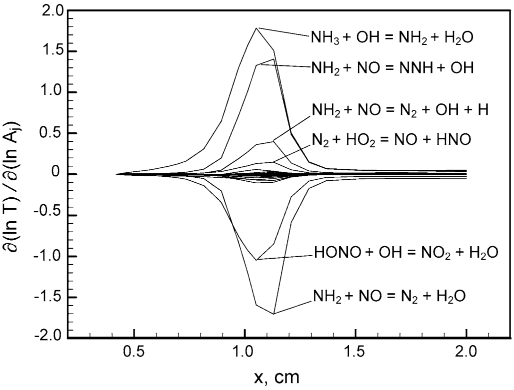

Fig. 13. Sensitivity coefficient of temperature with respect to chemical reactions for ADN combustion at 6 atm.

of 850–1250 K. The temperature range at the end of the secondary flame is about 1250–1650 K and no final flame is detected [6]. The reported final flame temperature below 40 atm never reaches its counterpart of about 2070 K at 60 atm [6], possibly due to heat loss to the ambient environment. In the experiments performed by Korobeinichev et al. [9], however, the measured final flame temperature at 40 atm is about 2000 K. The dominant species at the end of the secondary flame are mainly NO, N_2O, N_2, and H_2O [63]. Hence, it is reasonable to consider the reaction zone after the secondary flame of ADN as a second dark-zone temperature plateau similar to that in the DB and nitramine propellant combustion with a temperature range of 1200–1600 K.

$NH_3 + NO_x$ reactions have been extensively studied [66–75] in the past decade, and they have been found to exert a significant influence on the combustion chemistry and the dark-zone characteristics of ADN. Reactions (R19), (R33), and (R57)–(R64) are important in the $NH_3 + NO_2$ system. In the primary-flame zone, the global reaction of NH_3 and NO_2 is believed to be a major source of heat release [64]. Park and Lin [70] observed that in the reaction system of $NH_3 + NO_2$, the species-concentration profiles exhibited two different regimes. Below 660 °C, concentrations of NH_3 and NO_2 decreased quickly, and those of NO and N_2O increased rapidly with increasing temperature. Above 660 °C, variations in species concentration tended to diminish. There seemed a plateau zone for NO concentration with increasing temperature. It was noted that the reduction of NO_x by NH_3 was the most sensitive to the NH_2 radical reactions. The species NO has a tendency to inhibit the reaction by destroying the NH_2 radicals and forming stable N_2 and H_2O species by (R33) [66–69]. The experimental data obtained by Bedford and Thomas [68] and calculations by Thaxton et al. [69] showed that the addition of NO significantly decreased the decay rate of NO_2. Thus, NO accumulation may cause the reduction of NH_2 radicals and affect the propagation of chain reactions. Reaction (R33) inhibits the chain reaction, whereas (R19) propagates the chain reaction by producing an OH radical. Reaction (R57) is considered a sensitive initial step, and the branching ratio of (R33) to (R19) is critical. According to Park and Lin [71–73], the branching ratio of (R33) to (R19) was 0.9/0.1 at 300 K and 0.78/0.28 at 1000 K, respectively. Above 1000 K, the ratio sharply decreased with increasing temperature.

$$NH_3 + NO_2 = NH_2 + HNO_2, \tag{R57}$$

$$NH_2 + NO_2 = NH + HNO_2, \tag{R58}$$

$$NH_2 + NO_2 = N_2O + H_2O, \tag{R59}$$

$$NH + NO_2 = HNO + NO, \tag{R60}$$

$$2HNO = H_2O + N_2O, \tag{R61}$$

$$NH_2 + NO = N_2 + H_2O, \tag{R33}$$

$$NH_2 + NO = N_2H + OH, \tag{R19}$$

$$2HNO_2 = NO_2 + NO + H_2O, \tag{R62}$$

$$HNO_2 + M = OH + NO + H_2O, \tag{R63}$$

$$HNO_2 + OH = NO_2 + H_2O. \tag{R64}$$

Liau et al. [65] performed a numerical analysis on the sensitivity of temperature and species-concentrations for ADN combustion. The sensitivity coefficient was defined as

$$S_{ij}(x) = \frac{\partial(\ln X_i)}{\partial(\ln A_j)}, \tag{13}$$

where X_i is the temperature or the mole fraction of species i, A_j the kinetic prefactor of reaction j, and x the distance from the propellant surface. Fig. 13 shows that (R19) had a positive effect, whereas (R33) had a negative effect on the gas-phase temperature, and $\partial(\ln T)/\partial(\ln A)$ reached a maximum value at

Table 11
Measured and predicted mole fractions of dark-zone species for self-sustained and laser-assisted combustion of ADN propellant

Propellant	NO	NH_3	N_2	H_2O	N_2O	HNO_2	NO_2	HNO_3	O_2	Ref.
Second dark zone (6 atm)[a] $L_d = 14$ mm $T_d = 1460$ K	0.26	0.012	0.1	0.42	0.22			∼0		[9]
Second dark zone (6 atm)[b] $L_d = 14$ mm $T_d = 1510$ K	0.17	0	0.17	0.40	0.26			0		[8,65]
First dark zone (3 atm)[a] $L_d = 2$ mm $T_d = 810$ K	0.16	0.07	0.08	0.31	0.25	0.03	0.03	0.08		[8]
First dark zone (3 atm)[b] $L_d = 2$ mm $T_d = 785$ K	0.143	0.10	0.085	0.29	0.235			0.075		[8]
Second dark zone (3 atm)[a,c] $\dot{q}''_{\text{laser}} = 100\ \text{W/cm}^2$ $T_d = 1328$ K	0.191	0.003	0.155	0.435	0.179				0.019	[7]
Second dark zone (5 atm)[a,c] $\dot{q}''_{\text{laser}} = 200\ \text{W/cm}^2$ $T_d = 1385$ K	0.162	0.012	0.169	0.435	0.184				0.019	[7]

[a] Experimental measurement.
[b] Numerical modeling.
[c] Laser-assisted combustion.

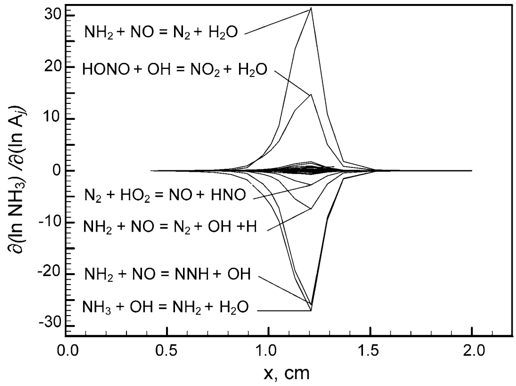

Fig. 14. Sensitivity coefficient of NH_3 with respect to chemical reactions for ADN combustion at 6 atm.

about 11 mm from the surface. For NH_3, the effect of (R33) was positive, whereas the effect of (R19) was negative, and $\partial(\ln NH_3)/\partial(\ln A)$ had a maximum at about 12 mm from the surface, as shown Fig. 14. Reaction (R33) exerted a negative effect on the H_2O concentration, whereas the influence of (R19) was positive. Reaction (R47) was the most sensitive with respect to the variations in temperature and concentration profiles of H_2O and N_2O, as it produces the NH_2 radical. The maximum value of $S_{ij}(x)$ occurred at 11–12 mm from the propellant surface, a position slightly above the secondary flame.

The existence of the first dark-zone temperature plateau in the range of 850–1250 K may be attributed to the inhibition in the progress of the exothermic reaction between NH_3 and NO_2 by the species NO. The second dark-zone temperature plateau at the end of the secondary flame can be explained on the basis of high concentrations of NO and N_2O which undergo reactions that require high activation energies. Table 11 summarizes the dark-zone species concentrations for ADN combustion at various pressures. The model predictions [8,65] are in good agreement with experimental results [8,9].

4. Sensitivity of dark-zone formation to physical parameters

A higher flow velocity in the gas phase causes the dark zone to be stretched, as the intermediate species are able to travel a longer distance prior to the occurrence of exothermic reactions. In most cases, the dark zone exists in the range 1–50 atm and disappears at higher pressures. The decrease in the flame-standoff distance with increasing pressure mainly results from the increase in the gas density ρ_g. It is worth noting that the transport velocity of the gas mixture ejected from the surface does not increase, but rather decreases slightly with increasing pressure, despite the enhanced burning rate. The data given in Table 12

Table 12
Burning properties of RDX/PU = 80/20 propellant [22]

Pressure, atm	15	20	30
Burning rate, cm/s	0.085	0.11	0.15
Surface temperature, K	670	680	690
Density at surface[a], kg/m^3	7.94	10.6	15.9
Velocity at surface[b], cm/s	17.1	16.6	15.1
Flame-standoff dist., cm	0.54	0.3	0.12

[a] Calculated using the NASA chemical equilibrium code.
[b] Calculated assuming propellant density of 1.6 g/cm^3.

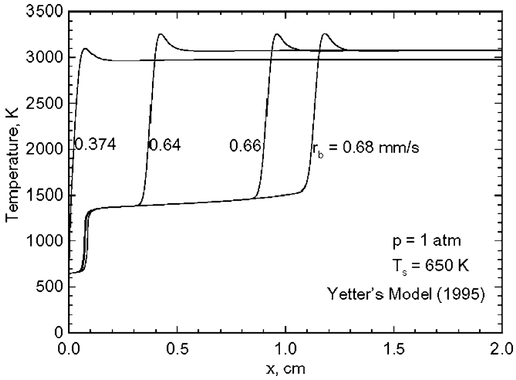

Fig. 15. Effect of propellant burning rate on temperature profile of RDX combustion.

elaborates this point. Such a phenomenon can be attributed to the fact that the density increases faster than the burning rate at a higher pressure. Thus, the increase of reactant concentrations and decrease of transport velocity both contribute to the reduction of the flame-standoff distance with increasing pressure.

A parametric study by Liau et al. [17] on RDX monopropellant combustion clearly shows the strong influence of burning rate, propellant surface temperature, and flow expansion on the dark-zone characteristics. In Fig. 15, the temperature increases monotonically without any plateau at a low burning rate of 0.374 mm/s. If the burning rate is greater than 0.64 mm/s, however, the combustion wave is stretched to form a dark-zone temperature plateau. Further increase in the burning rate extends the temperature plateau. An increase in the burning rate r_b amounts to an increase in the gas transport velocity V_d, according to Eq. (2). Thus, there exists a critical value of r_b to establish a noticeable dark zone for a given pressure. Fig. 16 shows the effect of propellant surface temperature on the temperature evolution in the gas phase. The shorter chemical induction time associated with a higher surface temperature reduces the dark-zone thickness. Results presented in Figs. 15 and 16 are based on the assumption of constant flame area. In reality, the flame expands laterally as the flow travels downstream from the propellant surface, as evident in Figs. 1 and 2. Such an expansion process effectively reduces the local gas transport velocity, and consequently shortens the dark zone. Fig. 17 shows the influence of the flame-area expansion. An artificial increase of the flame area by a factor of 2.4 almost eliminated the existence of a dark-zone temperature plateau. Davidson and Beckstead [18] adopted an optimal area expansion correlation in their modeling of RDX combustion to obtain a better agreement between the measured temperature profiles and propellant burning rates. Flame-area expansion, thus, is an important parameter in determining the extent of the dark-zone length.

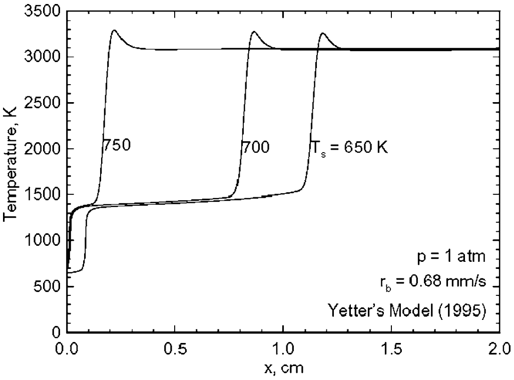

Fig. 16. Effect of propellant surface temperature on profile of RDX combustion.

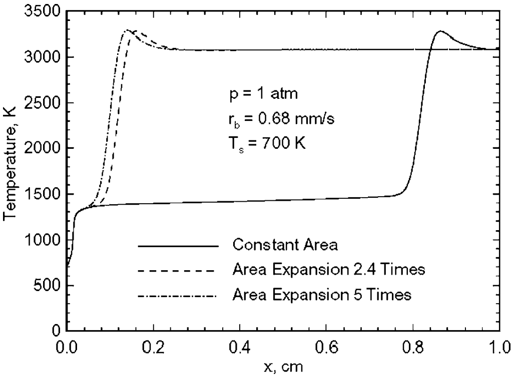

Fig. 17. Effect of flame-area expansion on temperature profile of RDX combustion.

Only limited studies are available regarding the effect of propellant preconditioned temperature, T_i, on the dark-zone behavior. The modeling results of Bizot and Beckstead [28] for DB propellant combustion indicated that L_d decreases as T_i increases from −20 to 60 °C, showing good agreement with experimental data. On the other hand, the study on ADN combustion by Zenin et al. [6] showed that L_d increases slightly from 2 to 2.5 mm as T_i varies from −150 to 20 °C at 20 atm. The different trends of L_d

with respect to T_i for DB and ADN propellants may be attributed to the different chemical pathways and species in their respective dark-zone regions.

For laser-assisted combustion, the primary flame and dark zone are known to stretch, mainly due to the enhanced transport and chemical effects. In the experiments on RDX combustion by Hanson-Parr and Parr [12,13], a dark-zone temperature plateau was clearly observed. Such a plateau, however, disappeared under self-deflagrated conditions, a phenomenon also predicted by the analyses given in [16,57]. Laser heating tends to increase the burning rates and surface temperatures of RDX and HMX [42,43]. Therefore, the resultant stretching effect on the dark zone can be attributed to the increase in the gas velocity and the dominance of the reaction mechanism (R2) over (R1) at higher heat flux. The combustion of nitramine-based composite propellants exhibited a more noticeable dark zone than RDX and HMX monopropellants. XM39 (RDX 76%, cellulose acetate butyrate (CAB) 12%, nitrocellulose (NC) 4%) has a longer flame-standoff distance under self-deflagration at 1 atm [45]. It is believed that the gaseous products from the inert binders dilute the concentrations of the reactive species above the propellant surface and thus stretch the dark zone.

For pure AP and AP-based composite propellants, no dark zone is observed at atmospheric pressure and above. Krishnan and Jeenut [11], however, reported the existence of a dark zone for the combustion of nonmetallized AP/HTPB composite propellant with copper chromite as a catalyst in nitrogen, under subatmospheric pressures ($\sim 10^{-2}$ bar). The dark-zone thickness increased with increasing concentration of copper chromite and decreasing pressure or AP particle size. Korobeinichev [8] also studied the combustion characteristics of pure AP and AP/HTPB propellants at low pressures ($\sim$0.5 atm) using a microprobe technique along with a modeling work. Results of measured and predicted species concentration profiles suggested that the AP flame exhibits a two-zone structure: a narrow zone ($\sim$0.1 mm) where NH_3, $HClO_4$, and ClO_2 concentrations decrease and NO_2 concentration increases; and a wide zone ($\sim$1.5 mm) where NO_2 concentration decreases while NO and O_2 concentrations increase. The AP/HTPB composite propellant exhibited a similar two-zone feature. Although Korobeinichev did not describe it as a dark zone, the wide zone could be interpreted as a dark zone at low pressures.

In light of the aforementioned discussions, a dark zone exists in homogeneous propellants under low and moderate pressures. Owing to the strong oxidation of AP decomposition products, combustion of oxidizer-rich AP generates a diffusion flame and does not produce a dark zone at atmospheric pressure and above. When pressure is as low as 24 mbar, however, a dark zone is observed [11]. The phenomenon may be attributed to the fact that AP and AP/HTPB propellant combustion becomes kinetically controlled under very low pressures, similar to those of homogeneous propellants.

5. Conclusions

The key physiochemical mechanisms involved in the formation of a dark zone in solid-propellant combustion have been investigated for a variety of propellants. Emphasis was placed on the sensitivity of the dark-zone behavior to various chemical pathways and physical parameters. The existence of a dark-zone temperature plateau can be attributed to the presence of species such as HCN, NO, CO, and N_2O, which undergo reactions involving high activation energies. The species require a finite residence time commensurate with the chemical induction time to complete their reactions. The chemical and transport processes of the intermediate species thus play a vital role in the formation of a dark zone.

A dark zone is usually observed in the combustion of homogeneous propellants up to 60 atm, and its length can be correlated with pressure in the form of $L_d = ap^d$. High gas-mixture velocity above the propellant surface favors the formation of a dark zone. Higher surface and preconditioned temperatures of propellants reduce the dark-zone thickness due to the decrease in the chemical induction time. Under laser-assisted conditions, the primary flame and dark zone in RDX monopropellant combustion are known to stretch due to enhanced transport and chemical effects. Such phenomenon can be attributed to the increase in the gas velocity and the dominance of the reaction mechanism RDX_l (HMX_l) $\rightarrow$ 3(4) ($H_2CN + NO_2$) (R2) over RDX_l (HMX_l) $\rightarrow$ 3(4) ($CH_2O + N_2O$) (R1) under intensive heating.

NO is a critical species in the dark zones of most solid propellants. Other important species include CO for DB propellants, HCN for nitramine propellants, and N_2O for ADN propellants. For DB and nitramine propellants, the dark-zone temperature plateau usually ranges between 1200 and 1600 K, in which species concentrations vary moderately. ADN combustion exhibits two dark zones. The formation of the first dark zone (850–1250 K) near the propellant surface results from the NO inhibition effect in the reaction between NH_3 and NO_2. The second dark zone at the end of the secondary flame arises from the high concentrations and weak reactivities of NO and N_2O. The second dark zone in ADN combustion is similar in nature to those observed in nitramine and DB propellant combustion.

For nitramine propellants, the most sensitive reactions affecting the dark-zone characteristics are those proposed in the Yetter95 mechanism: $H_2CNNO_2 + NO_2 = CH_2O + N_2O + NO_2$ (R9), $H_2CNNO_2 + N_2O = CH_2O + N_2O + N_2O$ (R10), and $H_2CNNO_2 + H_2O = CH_2O + N_2O + H_2O$ (R11), as well as the following elementary reactions: $HCN + OH = HNCO + H$ (R13), $HNO + OH = H_2O + NO$ (R18), $NH_2 + NO = N_2H + OH$ (R19), $N_2H + NO = HNO + N_2$ (R20), $HNCO + H = NH_2 + CO$ (R21), $HNO + NO = N_2O + OH$ (R32), $NH_2 + NO = N_2 + H_2O$ (R33), $HNC + OH = HNCO + H$ (R34), $HNCO + CN = HCN + NCO$ (R35), and $HCN = HNC$ (R36). In the case of DB propellants, the most sensitive reactions in the dark zone are (R32) and $N_2O + O = NO + NO$ (R48), and for ADN propellants, they are (R19), (R33), $NH_3 + OH = NH_2 + H_2O$ (R47), and $NH_3 + NO_2 = NH_2 + HNO_2$ (R57).

Acknowledgments

This work was supported partly by Pennsylvania State University and partly by the subcontract from Software Engineering Associates (SEA), Carson City, NV, funded by ONR Contract N00014-02-C-0292, Judah Goldwasser as Contract Monitor. The authors are deeply grateful to William Anderson for extensive discussions on the subject material.

References

[1] G. Lengellé, A. Bizot, J. Duterque, J.F. Trubert, in: V. Yang, T.B. Brill, W.-Z. Ren (Eds.), Solid Propellant Chemistry, Combustion, and Motor Interior Ballistics, Progress in Astronautics and Aeronautics, vol. 185, 2000, pp. 287–334.

[2] N. Kubota, in: K.K. Kuo, M. Summerfield (Eds.), Fundamentals of Solid-Propellant Combustion/Progress in Astronautics and Aeronautics, vol. 90, American Institute of Aeronautics and Astronautics, 1984, pp. 1–52.

[3] J.A. Vanderhoff, A.J. Kotlar, S.H. Modiano, M.W. Teague, in: K.K. Kuo, T.B. Brill, R.A. Pesce-Rodriguez, A.R. Mitchell, J. Covino, S.K. Chan, A. Peretz, N.-E. Gunners, S.T. Thynell, S.H. Chan (Eds.), Challenges in Propellants and Combustion/100 Years after Nobel, Begell House, New York, 1997, p. 807.

[4] T.P. Parr, D. Hanson-Parr, in: V. Yang, T.B. Brill, W.-Z. Ren (Eds.), Solid Propellant Chemistry, Combustion, and Motor Interior Ballistics, Progress in Astronautics and Aeronautics, vol. 185, 2000, pp. 381–411.

[5] T.A. Litzinger, Y.-J. Lee, C.-J. Tang, in: V. Yang, T.B. Brill, W.-Z. Ren (Eds.), Solid Propellant Chemistry, Combustion, and Motor Interior Ballistics, Progress in Astronautics and Aeronautics, vol. 185, 2000, pp. 355–379.

[6] A.A. Zenin, V.M. Puchkov, S.V. Finjakov, AIAA Paper 99-0595, 1999, pp. 1–9.

[7] B.L. Fetherolf, T.A. Litzinger, Combust. Flame 114 (1998) 515.

[8] O.P. Korobeinichev, in: V. Yang, T.B. Brill, W.-Z. Ren (Eds.), Solid Propellant Chemistry, Combustion, and Motor Interior Ballistics, Progress in Astronautics and Aeronautics, vol. 185, 2000, pp. 335–354.

[9] O.P. Korobeinichev, L.V. Kuibida, A.A. Paletsky, A.G. Shmakov, AIAA Paper 98-0445, 1998, pp. 1–11.

[10] A.E. Fogelzang, V.P. Sinditskii, V.Y. Egorshev, A.I. Levshenkov, in: 28th International Annual Conference of ICT, Karlsruhe, FRG, 1997, pp. 99.1–99.14.

[11] S. Krishnan, R. Jeenut, J. Propuls. Power 8 (1992) 748.

[12] T.P. Parr, D.M. Hanson-Parr, in: T.B. Brill, T.P. Russell, W.C. Tao, R.B. Wardle (Eds.), Decomposition, Combustion, and Detonation Chemistry of Energetic Materials/Materials Research Society Symposium Proceedings, vol. 418, 1996, p. 207.

[13] D. Hanson-Parr, T.P. Parr, Proc. Combust. Inst. 25 (1994) 1635.

[14] Y. Lee, C.-J. Tang, T.A. Litzinger, Combust. Flame 117 (1998) 600.

[15] T.A. Litzinger, B.L. Fetherolf, Y.-J. Lee, C.-J. Tang, J. Propuls. Power 11 (1995) 698.

[16] Y.-C. Liau, V. Yang, J. Propuls. Power 11 (1995) 729.

[17] Y.-C. Liau, E.S. Kim, V. Yang, Combust. Flame 126 (2001) 1680.

[18] J.E. Davidson, M.W. Beckstead, J. Propuls. Power 13 (1997) 375.

[19] K. Prasad, R.A. Yetter, M.D. Smooke, Combust. Flame 115 (1998) 406.

[20] N. Kubota, Proc. Combust. Inst. 17 (1978) 1435.

[21] N. Kubota, T. Sonobe, Proc. Combust. Inst. 23 (1990) 1331.

[22] N. Kubota, Proc. Combust. Inst. 18 (1981) 187.

[23] N. Kubota, X. Hirata, Proc. Combust. Inst. 21 (1986) 1943.

[24] Y. Yano, N. Kubota, Propell. Explos. Pyrot. 10 (1985) 192.

[25] G. Nakashita, N. Kubota, Propell. Explos. Pyrot. 16 (1991) 177.

[26] D. Hanson-Parr, T. Parr, in: 26th JANNAF Combustion Meeting, CPIA Publication 529, vol. I, 1989, p. 27.

[27] T.-S. Roh, I.-S. Tseng, V. Yang, J. Propuls. Power 11 (1995) 640.

[28] A. Bizot, M.W. Beckstead, Proc. Combust. Inst. 22 (1988) 1827.

[29] R.A. Fifer, A.J. Kotlar, M.S. Miller, J.B. Morris, in: 27th JANNAF Combustion Subcommittee Meeting, CPIA Publication 557, vol. I, 1990, p. 95.

[30] N. Ilincic, W.R. Anderson, K. Seshadri, N.E. Meagher, Proc. Combust. Inst. 26 (1996) 1997.

[31] A. Zenin, J. Propuls. Power 11 (1995) 752.

[32] C.F. Melius, in: S.N. Bulusu (Ed.), Chemistry and Physics of Energetic Materials, Kluwer Academic, 1990, p. 51.

[33] R.A. Yetter, F.L. Dryer, M.T. Allen, J.L. Gatto, J. Propuls. Power 11 (1995) 683.

[34] J.A. Miller, C.T. Bowman, Prog. Energy Combust. Sci. 15 (1989) 287.

[35] D. Chakraborty, M.C. Lin, in: V. Yang, T.B. Brill, W.-Z. Ren (Eds.), Solid Propellant Chemistry, Combustion,

and Motor Interior Ballistics, Progress in Astronautics and Aeronautics, vol. 185, 2000, pp. 33–71.

[36] Y.-C. Liau, V. Yang, AIAA Paper 97-0589, 1997, pp. 1–12.

[37] T.B. Brill, J. Propuls. Power 11 (1995) 740.

[38] W.R. Anderson, N. Ilincic, N.E. Meagher, K. Seshadri, J.A. Vanderhoff, in: 32nd JANNAF Combustion Meeting, CPIA Publication 638, vol. I, 1995, p. 197.

[39] R.J. Kee, J.F. Grcar, M.D. Smooke, J.A. Miller, Sandia National Laboratories Report No. SAND85-8240, 1985.

[40] N.E. Ermolin, O.P. Korobeinichev, L.V. Kuibida, Combust. Explosion Shock Wave 24 (1988) 400.

[41] J.A. Vanderhoff, W.R. Anderson, A.J. Kotlar, in: 29th JANNAF Combustion Subcommittee Meeting, CPIA Publication 593, vol. II, 1992, p. 225.

[42] C.-J. Tang, Y.J. Lee, G. Kudva, T.A. Litzinger, Combust. Flame 117 (1999) 170.

[43] Y.J. Lee, C.-J. Tang, T.A. Litzinger, Combust. Flame 117 (1999) 795.

[44] C.A. Heller, A.S. Gordon, J. Phys. Chem. 59 (1955) 773.

[45] G. Kudva, C.-J. Tang, Y.J. Lee, T.A. Litzinger, in: 33rd JANNAF Combustion Subcommittee Meeting, CPIA Publication 653, vol. II, 1996, p. 569.

[46] C.-J. Tang, T.A. Litzinger, in: 34th JANNAF Combustion Subcommittee Meeting, CPIA Publication 662, vol. II, 1997, p. 481.

[47] E.S. Kim, V. Yang, Y.-C. Liau, Combust. Flame 131 (2002) 227.

[48] J.E. Davidson, M.W. Beckstead, Proc. Combust. Inst. 26 (1996) 1989.

[49] T.P. Parr, D.M. Hanson-Parr, in: 32nd JANNAF Combustion Subcommittee Meeting, CPIA Publication 631, vol. I, 1995, p. 429.

[50] J.A. Vanderhoff, M.W. Teague, A.J. Kotlar, in: 30th JANNAF Combustion Meeting, CPIA Publication 606, vol. II, 1993, p. 465.

[51] J. Wormhoudt, P.L. Kebabian, C.E. Kolb, Combust. Flame 111 (1997) 73.

[52] B.L. Fetherolf, T.A. Litzinger, Y.-C. Lu, K.K. Kuo, in: 30th JANNAF Combustion Subcommittee Meeting, CPIA Publication 606, vol. II, 1993, p. 183.

[53] Y.-C. Liau, V. Yang, in: V. Yang, T.B. Brill, W.-Z. Ren (Eds.), Solid Propellant Chemistry, Combustion, and Motor Interior Ballistics, Progress in Astronautics and Aeronautics, vol. 185, 2000, pp. 477–500.

[54] B.E. Homan, M.S. Miller, J.A. Vanderhoff, Combust. Flame 120 (2000) 301.

[55] T.P. Parr, D.M. Hanson-Parr, Proc. Combust. Inst. 27 (1998) 2301.

[56] M.S. Miller, W.R. Anderson, ARL-TR-2167, 2000, pp. 1–18.

[57] M.S. Miller, W.R. Anderson, in: V. Yang, T.B. Brill, W.-Z. Ren (Eds.), Solid Propellant Chemistry, Combustion, and Motor Interior Ballistics, Progress in Astronautics and Aeronautics, vol. 185, 2000, pp. 501–531.

[58] W.R. Anderson, N. Ilincic, K. Seshadri, in: 31st JANNAF Combustion Subcommittee Meeting, CPIA Publication 412, vol. I, 1994, p. 1.

[59] M.W. Teague, G. Singh, J.A. Vanderhoff, in: 30th JANNAF Combustion Subcommittee Meeting, CPIA Publication 606, 1993, vol. II, p. 217.

[60] G. Lengelle, in: K.K. Kuo, T.B. Brill, R.A. Pesce-Rodriguez, A.R. Mitchell, J. Covino, S.K. Chan, A. Peretz, N.-E. Gunners, S.T. Thynell, S.H. Chan (Eds.), Challenges in Propellants and Combustion/100 Years after Nobel, Begell House, New York, 1997, p. 515.

[61] M.C. Lin, J. Park, Proc. Combust. Inst. 27 (1998) 2351.

[62] V.A. Strunin, A.P. D'Yakov, G.B. Manelis, Combust. Flame 117 (1999) 429–434.

[63] O.P. Korobeinichev, T.A. Bolshova, A.A. Paletsky, Combust. Flame 126 (2001) 1516–1523.

[64] T.B. Brill, P.J. Brush, D.G. Patil, Combust. Flame 92 (1993) 178–186.

[65] Y.-C. Liau, V. Yang, M.C. Lin, J. Park, in: 35th JANNAF Combustion Subcommittee Meeting, CPIA Publication 680, 1998.

[66] W.A. Rosser Jr., H.J. Wise, J. Chem. Phys. 29 (1956) 1078.

[67] F. Falk, R.N. Pease, J. Am. Chem. Soc. 76 (1954) 4746.

[68] G. Bedford, J.H. Thomas, J. Chem. Soc. Faraday Trans. I 68 (1972) 2163.

[69] A.G. Thaxton, C.-C. Hsu, M.C. Lin, Int. J. Chem. Kinet. 29 (1997) 245.

[70] J. Park, M.C. Lin, Int. J. Chem. Kinet. 28 (1996) 879.

[71] J. Park, M.C. Lin, J. Phys. Chem. A 101 (1997) 5.

[72] J. Park, M.C. Lin, J. Phys. Chem. A 101 (1997) 2643.

[73] J. Park, M.C. Lin, J. Phys. Chem. A 100 (1996) 3317.

[74] A.M. Mebel, M.C. Lin, Int. Rev. Phys. Chem. 16 (1997) 249.

[75] P. Glarborg, K. Dam-Johansen, J.A. Miller, Int. J. Chem. Kinet. 26 (1994) 421.

[76] B.E. Homan, J.A. Vanderhoff, Appl. Spectrosc. 53 (7) (1999) 816–821.